

Numerical analysis of inductively coupled plasma torch dynamics for titanium particle spheroidization using Python

Hendrik J. Greeff^{a*}, Samuel A. Iwarere^a, Hertzog Bisset^b

^a Department of Chemical Engineering, Faculty of Engineering, Built Environment and Information Technology, University of Pretoria, Hatfield, Pretoria 0028, South Africa

^b South African Nuclear Energy Corporation (Necsa), Church Street West Extension, Pelindaba, Broederstroom 0204, South Africa

Abstract

The growing demand for high-quality titanium powders in additive manufacturing requires advanced modelling of inductively coupled plasma (ICP) torches to optimize spheroidization. This study presents a Python-based multi-physics solver for the Tekna PL-50 ICP torch, simulating plasma behaviour and single-particle spheroidization. We use the standard technique (ST) for electromagnetic field equations, validated with <5% error. A finite-volume method with staggered hollow-cylindrical control volumes ensures stable thermo-fluid simulations, achieving <1.4% error in laminar benchmarks. At 5 kW, simulations reveal a central eddy and ~10,100 K peak temperature; 10–15 kW increases velocities to ~23 m/s with reduced temperature gains, narrowing processing windows. Swirl flow stabilizes the plasma-sheath interface by mitigating Lorentz-induced eddies, with inlet velocity variations proving negligible. Particle diameter dominates spheroidization: <500 µm particles spheroidize at 5 kW, 1000 µm remain unmelted, and <100 µm melt with >20% vaporization loss. Optimal conditions at ~4.5 kW (9,800 K) enable stable spheroidization up to 400 µm with minimal loss. This cost-effective solver offers an extensible alternative to commercial software. We recommend experimental validation at Necsa under dense particle loading and adaptive meshing for improved high-power accuracy, advancing plasma processing efficiency and powder quality in industrial applications.

Keywords: Thermal processing; Powder morphology; Plasma dynamics; Electromagnetic simulation; Flow stabilization

1. Introduction

Inductively coupled plasma (ICP) torches are widely used in powder metallurgy to refine particle morphology, enhance flowability, increase packing density and improve purity [1]. Their main application in this context is to spheroidize irregularly shaped refractory metals, intermetallics and ceramics; making them easier to handle and process. The spheroidization of particles is one of the successful commercial applications of ICP torches [2]. In the spheroidization process, fine powders are heated and melted, after which the liquid droplets become spherical under the effect of surface tension before resolidifying [3]. These spherical particles are easier to machine and has benefits such as increased powder flowability and packing density [2].

The ICP torch generates plasma through the electromagnetic coupling of radiofrequency (RF) energy with an inert gas medium – typically argon or helium – resulting in high-temperature, high-enthalpy conditions suitable for melting and reshaping particles [2]. The alternating current in the RF coil induces an oscillating magnetic field, which then generates eddy currents within the ionized gas, leading to ohmic heating that sustains the plasma.

Titanium and titanium alloys are a vital part of the aerospace and biomedical industries due to their low

density, high strength, and excellent corrosion resistance [4]. However, their high strength also presents challenges due to the difficulties they cause in manufacturing and machining products with complex geometries. Additive manufacturing (3D printing) techniques have emerged as a viable solution for producing complex components [4]. These techniques necessitate high-quality, spherical metal powders to ensure consistent flowability, uniform deposition, and minimal manufacturing defects. Consequently, significant research efforts are devoted to the production of specialized metallic powders [5, 6, 7]. RF-ICP torch technology is recognized as a reliable method for producing high-quality, spheroidized titanium powders for 3D printing applications [4].

Despite their advantages, ICP torches are challenging to measure and control, limiting their widespread industrial adoption [1,3]. Particle motion within an ICP torch involves complex interactions between plasma flow, electromagnetic fields, and thermal gradients, complicating experimental analysis. Numerical simulation presents a valuable tool for predicting spheroidization outcomes, enabling parametric studies that would otherwise be costly or impractical experimentally. Numerical modelling also addresses challenges such as high equipment costs and difficulties in direct in situ measurements of plasma conditions.

Most numerical models for ICP plasmas rely on expensive and inaccessible commercial software such as COMSOL and FLUENT. Developing a numerical model

* Corresponding author. Tel.: +27-079-783-0639; e-mail: u22534114@tuks.co.za.

in a Python environment offers a cost-effective and flexible alternative, enhancing accessibility and facilitating broader research efforts.

At the South African Nuclear Energy Corporation SOC Ltd (Necsa), ICP technology is employed to spheroidize irregular metallic particles. Key parameters influencing spheroidization efficiency include the plasma temperature profile, plasma shape, and particle residence time within the plasma. Commercial software packages are prohibitively expensive and inaccessible for routine research at Necsa. Therefore, this project aims to develop a numerical model of plasma-particle interactions within a Python environment, thereby improving the understanding of spheroidization dynamics and offering an accessible alternative to commercial software.

The primary research questions are whether a Python-based model can accurately predict the plasma temperature and velocity profiles within an ICP torch, and whether this model can reliably forecast the spheroidization behaviour of metallic particles.

The aim of this work is to develop this numerical model in a Python environment that accurately simulates the electromagnetic and thermo-fluid dynamics of an RF-ICP torch and predicts metallic particle spheroidization. This will provide an accessible alternative to commercial modelling tools. To accomplish this, key objectives involve developing Python-based numerical code for electromagnetic and thermo-fluid simulations. This code solves Maxwell's equations in conjunction with the Navier-Stokes and energy equations to precisely model the plasma's electromagnetic field, temperature distribution, and velocity profiles. Furthermore, a particle trajectory and heat transfer module is integrated into the model to predict if a single injected particle will spheroidize under given plasma conditions.

This work models the ICP torch by decoupling the flow equations from the electromagnetic field equations. The flow equations are solved on a separate unstructured grid using the finite volume method, and the electromagnetic field equations are solved using the vector potential formulation with the standard technique on a separate structured grid via the finite difference method. This model is built on an axisymmetric grid. The particle dynamics are modelled using one-directional single particle dynamics.

2. Model

Fig. 1 shows the layout of a Tekna PL-50 torch that was considered in this study. The dimensions and operating conditions are shown in Table 1. The plasma discharge is sustained inside a quartz tube with three coaxial inlets: a central carrier for particle injection, a main plasma-forming stream, and an outer sheath that cools the wall and stabilises the jet. The outer stream is often operated with a tangential component [8] and in this work the swirl was

required to obtain stable results. The rest of the model was completed in a two-dimensional, axisymmetric formulation. The induction system is represented by three parallel circular current loops surrounding the main tube; the helical pitch and axial current components are neglected. Pure argon is used as working gas in all streams.

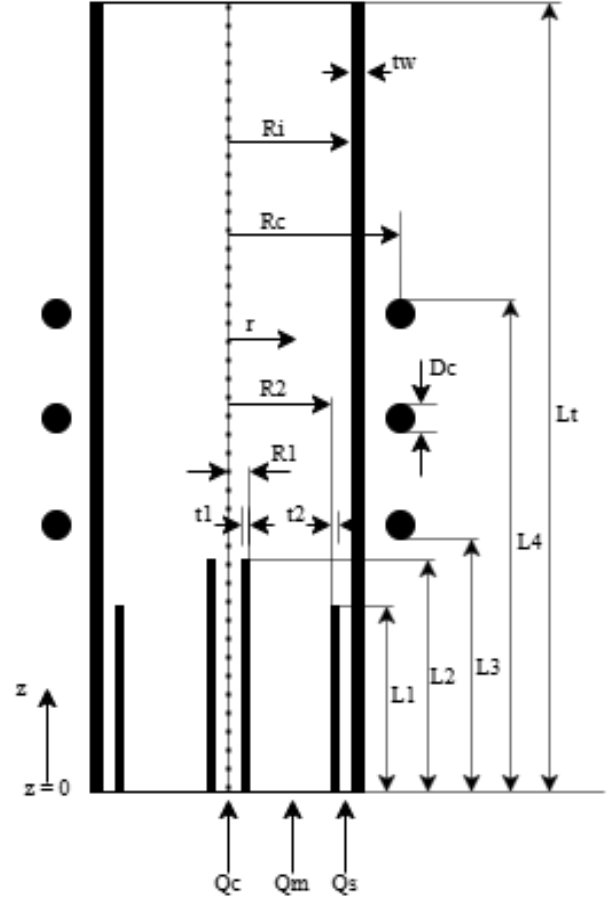


Fig. 1. Schematic of the Tekna PL-50 torch.

Table 1
TEKNA PL-50 plasma torch parameters.

Parameter	Value	Unit	Parameter	Value	Unit
L_t	200	mm	t_1	2	mm
L_1	50	mm	t_2	2.2	mm
L_2	50	mm	t_w	6	mm
L_3	60	mm	D_c	6	mm
L_4	124	mm	Q_c	1	slpm
R_c	33	mm	Q_m	3	slpm
R_1	3.7	mm	Q_s	31	slpm
R_2	18.8	mm	P	5	kW
R_i	25	mm	f	3	MHz

Thermophysical properties of argon are treated as functions of temperature at 1 atm: density $\rho(T)$, thermal conductivity $k(T)$, dynamic viscosity $\mu(T)$, and electrical conductivity $\sigma(T)$.

The general assumptions for the ICP torch model follow from established literature [8,9]:

- A two-dimensional axisymmetric geometry (r, z).
- The plasma is optically thin and in local thermodynamic equilibrium (LTE), implying electron temperature equals heavy particle temperature.
- The plasma is at atmospheric pressure with negligible internal pressure fluctuations.
- Laminar, compressible flow.
- The pressure work and viscous dissipation in the energy equation is negligible.
- The displacement current from oscillating magnetic fields is negligible.
- The coil is modelled as three parallel ring loops, neglecting axial current components.
- The thermo-fluid dynamics timescale significantly exceeds the electromagnetic field timescale, allowing for time-averaged electromagnetic field solutions.

Following these assumptions, the model is governed by a coupled set of electromagnetic and thermo-fluid equations, outlined below. The electromagnetic formulation supplies the time-averaged Joule heating and Lorentz force that act as source terms in the conservation laws for mass, momentum, and energy.

2.1. Plasma equations

The thermo-fluid behaviour is governed by the following equations:

$$\frac{\partial \rho}{\partial t} = -\nabla \cdot \rho \mathbf{u} \quad (1)$$

$$\rho \frac{\partial \mathbf{u}}{\partial t} + \rho \mathbf{u} \cdot \nabla \mathbf{u} = \nabla \cdot \mu \left(\nabla \mathbf{u} + \frac{\partial \mathbf{u}}{\partial x_i} \right) - \nabla p + \mathbf{F}_l \quad (2)$$

$$\rho c_p \frac{\partial T}{\partial t} + \rho c_p \mathbf{u} \cdot \nabla T = \nabla \cdot k \nabla T + P - Q_r \quad (3)$$

where \mathbf{u} , p and T are the gas velocity, pressure and temperature, respectively; Q_r , P and \mathbf{F}_l are the radiative heat loss, ohmic heating and Lorentz force density respectively; and ρ , c_p , μ , and k are the gas density, heat capacity, dynamic viscosity, and thermal conductivity, respectively.

The radiative heat loss, Q_r , is computed using the following radiative law [8]:

$$Q_r = 5600(T - 9500) + 181(T - 9500)^2 \quad (4)$$

where T is in Kelvin and Q_r is in W/m³. When T is less than 9,500 K, the radiative heat loss is zero.

The vector potential formulation (electromagnetic field equations):

$$\nabla^2 \mathbf{A} = -\mu_0 \mathbf{J}_{coil} + \mu_0 \sigma \frac{\partial \mathbf{A}}{\partial t} \quad (5)$$

$$\mathbf{E} = -\frac{\partial \mathbf{A}}{\partial t} \quad (6)$$

$$\mathbf{B} = \nabla \times \mathbf{A} \quad (7)$$

where \mathbf{A} is the vector potential, \mathbf{J}_{coil} is the current density of the coil, μ_0 is the magnetic permeability in a vacuum and σ is the electrical conductivity of the gas (and a very strong function of the plasma temperature). \mathbf{E} and \mathbf{B} are the electric field and the magnetic flux density, respectively.

The plasma torch operates at high frequencies, which means that the numerical solution in real-time of Eq. (5) is computationally expensive. However, the timescale of the electromagnetic field is much smaller than that of the fluid dynamics, and therefore, the time-averaged solutions of the Lorentz force density (\mathbf{F}_l) and ohmic heating (P) can be used in the thermo-fluid equations. Under the quasi-steady RF assumption, and starting from a harmonic excitation current $\mathbf{J}_{coil} = |\mathbf{J}_{coil}| \cos(\omega t)$, the Fourier transform applied to Eq. (5) is:

$$\nabla^2 \bar{\mathbf{A}} = -\mu_0 \bar{\mathbf{J}}_{coil} + j\omega \mu_0 \sigma \bar{\mathbf{A}} \quad (8)$$

where $\bar{\mathbf{J}}_{coil}$ and $\bar{\mathbf{A}}$ are the complex solutions of the coil current density and magnetic vector potential, respectively. ω is the harmonic frequency.

Discretizing Eq. (8) using the Finite-Difference-Method leads to an extensive system of equations that needs to be solved in the complex domain. Python contains libraries like *SciPy* and *NumPy* that have the capability to solve linear systems in the complex domain.

After the complex solution of the magnetic vector potential has been obtained from the system of equations, the Lorentz force, \mathbf{F}_l , and the ohmic heating, P , can be obtained from:

$$\frac{1}{r} \frac{\partial}{\partial r} \left(r \frac{\partial A_\theta}{\partial r} \right) + \frac{\partial^2 A_\theta}{\partial z^2} - \left(\frac{A_\theta}{r^2} + i\mu_0 \sigma \omega A_\theta \right) = -\mu_0 J_c \quad (9)$$

$$B_z = \frac{1}{r} \frac{\partial}{\partial r} (r A_\theta), \quad B_r = -\frac{\partial A_\theta}{\partial z}, \quad E_\theta = -i\omega A_\theta \quad (10)$$

$$P = \frac{1}{2} \sigma |E_\theta|^2 \quad (11)$$

$$F_r = \frac{1}{2} \sigma \text{Re}[E_\theta B_z^*], \quad F_z = -\frac{1}{2} \sigma \text{Re}[E_\theta B_r^*] \quad (12)$$

where $*$ denotes the complex conjugate and $\text{Re}[x]$ to the real part of complex number x .

2.2. Initial and boundary conditions

The initial and boundary conditions for the thermo-fluid equations were set according to the values provided in Table 2.

The inlet velocities were calculated assuming the standard litre per minute (slpm) is at 1 atm and 298 K, using the following equation:

$$u = \frac{Q}{A} \quad (13)$$

with Q the volume flowrate in m³/s and A the area in m².

A coil current of 150 A leads to a plasma operational power of 5 kW [8].

Table 2
Initial and boundary conditions for fluid dynamics.

Field Variable	Initial Condition	Boundary conditions
u	precomputed	Inlets: fixed $u_c = 1.84$ m/s, $u_m = 0.047$ m/s, $u_s = 0.894$ m/s; Walls: $u_r = u_z = 0$ m/s Axis: $u_r = 0, \partial u_z / \partial r = 0$ Outlet: $\frac{\partial u}{\partial n} = 0$
T	precomputed	Inlets and walls: fixed $T = 350$ K Outlet and axis: $\partial T / \partial n = 0$
p	$p = 1$ atm	Inlets, walls and axis: $\partial p / \partial n = 0$ Outlet: $p = 1$ atm

For the solution of Eq. (9), which is the axisymmetric formulation of Eq. (8), the boundary conditions are:

$$A_\theta(0, z) = 0 \quad (14)$$

$$A_\theta(R_b, Z_b) = f_1(A_\theta, r, z) + f_2(R_c, r, z) \quad (15)$$

$$f_1(A_\theta, r, z) = -\frac{i\omega\mu_0}{2\pi} \sum_{j=1}^{N_{cv}} (\sigma_j A_{\theta j}) \Delta S_j \sqrt{\frac{r_j}{R_b}} G(k_i) \quad (16)$$

$$f_2(R_c, r, z) = \frac{\mu_0 I_c}{2\pi} \sum_{i=1}^{N_c} \sqrt{\frac{R_i}{R_b}} G(k_i) \quad (17)$$

$$G(k) = \frac{(2-k^2)K(k)-2E(k)}{k} \quad (18)$$

$$k_j = \left[\frac{4r_j R_b}{(r_j + R_b)^2 + (Z_b - z_j)^2} \right]^{0.5} \quad (19)$$

$$k_i = \left[\frac{4R_i R_b}{(R_i + R_b)^2 + (Z_b - z_i)^2} \right]^{0.5} \quad (20)$$

where $K(k)$ and $E(k)$ are the elliptic integrals of the first and second type, respectively. The standard technique (ST) method was used to derive the analytical boundary conditions [8]. Importantly, Eq. (16) requires the value of the axial magnetic vector potential, A_θ , inside the domain. Therefore, the boundary conditions require the final value of A_θ and therefore the solution for the magnetic vector potential using the standard technique requires an iterative approach and an initial guess.

Other approaches exist and are outlined in literature [8]; however, analysis found that the ST approach provides results more efficiently with a good initial guess.

2.3. Pressure-correction

Since the pressure variations within the plasma are negligible, the continuity equation cannot be employed to solve the thermo-fluid dynamics in the torch. Coupling the plasma density ρ , to the plasma pressure p , through an equation of state will exacerbate numerical errors because of the negligible variations in the pressure.

Therefore, a pressure correction equation for variable density fluid was needed. This equation was adapted and

corrected from Colonna and D'Angola [9] and is provided below:

$$\nabla^2 p^{n+1} = \frac{\rho^{n+1} - \rho^n}{\Delta t^2} + \frac{\text{div}(\rho \mathbf{u}^*)}{\Delta t} \quad (21)$$

where Δt is the numerical time-step between time steps $n+1$ and n . Eq. (21) lies at the centre of the fluid dynamics solver developed in this work. This equation is used to ensure that the solution to the momentum equation (Eq. (2)) conforms to the continuity equation via the pressure field.

2.4. Single particle dynamics

Single particle dynamics can be solved by employing the Basset-Boussinesq-Oseen equation [4]. The radial and axial movement of the particles are expressed as follows:

$$\frac{du_p}{dt} = -\frac{3}{4} C_D (u_p - u) U_R \left(\frac{\rho}{\rho_p d_p} \right) \quad (22)$$

$$\frac{dv_p}{dt} = -\frac{3}{4} C_D (v_p - v) U_R \left(\frac{\rho}{\rho_p d_p} \right) + g_{eff} \quad (23)$$

where U_R is the relative slip velocity between the particle and gas:

$$U_R = \sqrt{(u_p - u)^2 + (v_p - v)^2} \quad (24)$$

u_p and v_p refer to the radial and axial velocity of the particle, respectively, and u and v are the radial and axial velocities of the fluid.

The gravitational term is corrected for buoyancy effects (which was omitted in [4]):

$$g_{eff} = g * \left(1 - \frac{\rho_{fluid}}{\rho_p} \right) \quad (25)$$

The drag coefficient C_D is expressed as a function of the particle Reynolds number, Re_p , and is valid for a sphere:

$$C_D = \begin{cases} 24/Re_p & Re_p \leq 0.2 \\ 24/Re_p * (1 + 0.1875 Re_p) & 0.2 < Re_p \leq 2.0 \\ 24/Re_p * (1 + 0.11 Re_p^{0.81}) & 2.0 < Re_p \leq 21.0 \\ 24/Re_p * (1 + 0.81 Re_p^{0.62}) & 21.0 < Re_p \leq 200 \end{cases} \quad (26)$$

The instantaneous energy balance assumes convection and radiation heat exchange with the plasma and is used to calculate the particle temperature, T_p :

$$\frac{dH_p}{dt} = \text{Convection} - \text{Radiation} \quad (27)$$

$$\text{Conv.} = A_p h_c (T - T_p) \quad (28)$$

$$\text{Rad.} = A_p \sigma_s \epsilon (T_p^4 - T^4) \quad (29)$$

$$A_p = \pi D_p^2 \quad (30)$$

where A_p is the particle area, d_p is the particle diameter, σ_s is the Stefan-Boltzmann constant, and ϵ is the particle surface emissivity.

For sensible heating ($T_p < T_m$ or $T_m < T_p < T_b$):

$$V_p \rho_p C_{p,pt} \frac{dT_p}{dt} = \text{Conv.} - \text{Rad.} \quad (31)$$

For melting ($T_p = T_{mp}$):

$$m_p H_m \frac{dx}{dt} = \text{Conv.} - \text{Rad.} \quad (32)$$

$$V_p = m_p * \left(\frac{1-x}{\rho_{p,solid}} + \frac{x}{\rho_{p,liquid}} \right) \quad (33)$$

$$D_p = \sqrt[3]{6V_p/\pi} \quad (34)$$

where x is the liquid fraction. For boiling ($T_p = T_b$):

$$-\rho_p \left(\frac{\pi}{2} D_p^2 \right) H_v \frac{dD_p}{dt} = \text{Conv.} - \text{Rad.} \quad (35)$$

The heat transfer coefficient h_c is obtained from the Nusselt correlation [4]:

$$Nu_p = \frac{h_c D_p}{k} = 2 + 0.515 Re_p^{0.5} \quad (36)$$

This model assumes the following:

- That the particles are spherical.
- That the injection velocity equals the carrier gas velocity.
- That the particle dynamics are determined solely by drag and gravity.
- Particle charging effects are neglected.
- The particle internal temperature is uniform ($Bi \ll 1$).
- Single particles are injected.

Although assuming sphericity seems inconsistent (the purpose is spheroidization), irregular particle shapes are prohibitively complex to model due to uncertain correlations for drag and heat transfer. Instead, the equivalent Sauter mean diameter ($d_{p,sv}$) is employed. This diameter preserves the surface-area-to-volume ratio of the particle, which controls both drag and convective heat transfer. As a result, the approximation yields realistic predictions. Moreover, since surface tension forces guarantee that a fully molten particle is spherical, the assumption becomes valid once spheroidization occurs.

A particle is considered spheroidized if it has fully melted (liquid fraction $x = 1$). Before this point, full spheroidization cannot be confirmed.

3. Methodology

A customized multi-physics solver was developed in Python to simulate the two-dimensional axisymmetric model of the Tekna PL-50 ICP torch. The electromagnetic field equations were solved using the standard technique (ST) [8] method on a rectangular grid, while the thermo-fluid equations were discretized via a finite volume approach on a staggered mesh. To efficiently calculate the electromagnetic fields induced by the RF coil, a finite difference scheme was implemented with iterative boundary conditions derived analytically. The electromagnetic domain extended to the torch boundaries, while the fluid mesh overlapped exactly with it. A novel

adaptive time-stepping strategy based on the CFL condition was introduced to stabilize the transient flow solver. Using this method, the solver operates in pseudo-transient mode until it reaches steady state. The implementation was validated against analytical benchmarks and literature data for the Tekna PL-50 torch.

3.1. Computational domain

The axisymmetric geometry reduced the problem to a 2D (r, z) plane. For the electromagnetic solver, a structured rectangular grid with $N_i \times N_j$ nodes was employed. The radial coordinate was offset to avoid the singularity at $r = 0$. Second-order central differences discretized the operators, and ST boundary conditions were applied at the outermost nodes.

The thermo-fluid equations were solved on a staggered unstructured finite-volume mesh in the same domain. The finite volume elements were hollow cylinders. Scalars (pressure p , temperature T) were stored at cell centres, radial velocity u on east/west faces, and axial velocity v on north/south faces. This arrangement prevented checkerboard oscillations. For the ICP torch, the domain included sheath and carrier gas inlets, with the injection probe spanning at least one cell to ensure resolution.

The grid scheme is shown in Fig. 2, with the regular structured grid on the left, the unstructured grid on the right, and the hollow-cylindrical finite volume element at the bottom left.

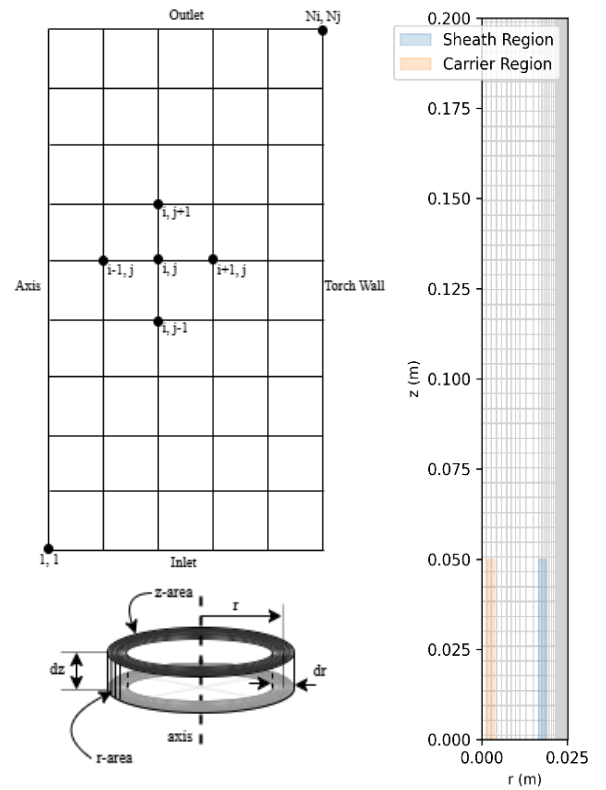


Fig. 2. Grid scheme used for the numerical analysis.

3.2. Electromagnetic field

Discretizing Eq. (9) leads to a linear system of equations with the following form for each interior node:

$$(K_1)A_{\theta i+1j} + (K_2)A_{\theta i-1j} + (K_3)A_{\theta ij+1} + (K_4)A_{\theta ij-1} + (K_5)A_{\theta ij} = 0 \quad (37)$$

$$\mathbf{D} \cdot \mathbf{A} = \mathbf{b} \quad (38)$$

where K_1 to K_5 are functions of the electrical conductivity $\sigma(T)$, radial position, and radial and axial spacing. The system in Eq. (38) is linear and A_θ (the solution) is complex. The system matrix D reduces to an identity matrix for boundary nodes and a five-diagonal stencil for interior nodes.

The value of the boundary nodes used in \mathbf{b} requires the values of A_θ at all interior points of the computational domain as can be seen from Eq. (15). Since Eq. (15) is non-local - linking boundary values to all interior values - the standard technique (ST) formulation must be solved iteratively. In practice, this is achieved by supplying an initial guess for A_θ and iterating until convergence, as outlined in Algorithm 1. Note that k refers to time step k and $k + 1$ to the next time step.

From the solution of A_θ the Lorentz force density and ohmic heating can be obtained.

Since the thermo-fluid equations are solved on an unstructured grid, linear interpolation was used to translate temperature (for electrical conductivity, σ) from the unstructured grid to the structured grid, and Lorentz force density and ohmic heating from the structured grid to the unstructured grid.

Algorithm 1: Magnetic vector potential solver

Set $A_\theta^k = A_\theta^0$

Start iterations

Look up σ from plasma temperature.

Assemble coefficient matrix D from conductivity field σ .

Assemble right-hand side \mathbf{b} using A_θ^k and ST boundary conditions.

Solve $\mathbf{D} \cdot \mathbf{A} = \mathbf{b}$ to find $A_{\theta k+1}$ with Bi - CGSTAB

Update $A_\theta^k = A_\theta^{k+1}$

Iterate until convergence.

End iterations

3.3. Thermo-fluid equations

The fluid solver treated the unsteady compressible Navier-Stokes and energy equations in flux form on an unstructured grid. An initial finite difference attempt on a collocated grid failed due to instabilities from $1/r$ terms and pressure-velocity decoupling. The finite volume

method resolved these issues by reformulating equations as flux balances, ensuring conservation, and the staggered grid eliminated odd-even coupling.

The solution algorithm is provided by Algorithm 2 and shows how the temporal dynamics of the thermo-fluid equations were determined. The continuity equation was not used – rather the pressure correction equation Eq. (21) was employed. Multiple pressure corrections were found to improve adherence of the velocity field to continuity: each iteration refines the tentative velocity field, reducing mass imbalance. The pressure–Poisson equation was assembled analogously to the electromagnetic matrix solver. Boundary conditions consisted of Neumann conditions on three sides of the domain and a Dirichlet condition to anchor pressure.

Algorithm 2: Finite Volume Solver

Set $T^k = T^0, \rho^k = \rho^0, u^k = u^0, v^k = v^0$

Start time loops

Compute Δt from CFL conditions.

Look up argon properties using T^k .

Solve Electromagnetic Field to find \mathbf{F}^k and P^k .

Find T^{k+1} using finite volume discretised energy equation.

Find the tentative velocity field, \mathbf{u}^* , using the finite volume discretised Navier-Stokes equations.

Find $\rho(T^{k+1})$ and solve $(\rho^{k+1} - \rho^k)/\Delta t^2$.

Start p -iterations

Calculate $\nabla \cdot \rho^{k+1} \mathbf{u}^*$

Solve the p correction equation.

Calculate $\rho^{k+1} \mathbf{u}^{k+1} = \rho^{k+1} \mathbf{u}^* - \Delta t \nabla p$

Calculate the residual of $(\rho^{k+1} - \rho^k)/\Delta t^2 - \nabla \cdot \rho^{k+1} \mathbf{u}^{k+1}$

Update boundaries.

Stop p -iterations

Set $T^{k+1} = T^k, \rho^{k+1} = \rho^k, u^{k+1} = u^k, v^{k+1} = v^k, p^{k+1} = p^k$

Check if $t > t_{total}$

End iterations

All the governing equations were advanced explicitly; therefore, numerical stability was limited by the Courant-Friedrichs-Lewy (CFL) condition as well as viscous and thermal diffusion constraints. At each global iteration, the code evaluates three candidate time steps at every cell face and selects the most restrictive value across the domain. The limiting mechanisms are summarised in Table 3, where c is an empirical constant between 0 and 1, and Δx is the smallest grid spacing.

The hybrid differencing scheme blended central and upwind interpolation based on the Péclet number $|Pe| < 2$.

Table 3

CFL conditions

Limiting Mechanism	Local Formula	Description
Convection	$\Delta t_{convection} = c\Delta x/ u_i $	Ensures that a fluid parcel does not travel more than one cell length Δx during a single time step.
Viscous diffusion	$\Delta t_{diffusion} = c\rho\Delta x^2/\mu$	Bounds momentum diffusion and guarantees positivity of the implicit viscosity matrix that arises in explicit integration.
Thermal diffusion	$\Delta t_{thermal} = c\rho c_p\Delta x^2/k$	Analogous to $\Delta t_{diffusion}$ but for thermal conduction.

Selecting realistic initial conditions is critical. At low temperatures argon’s electrical conductivity is several orders of magnitude too low for ohmic heating to initiate further ionisation. As a result, a quiescent start-up state of $T \approx 350$ K cannot evolve into a plasma without additional intervention. To address this, three complementary strategies were implemented:

1. Progressive temperature ramp: a localised heat source increases the core gas temperature by a small increment ΔT every few global iterations. Once the core reaches approximately 6000 K, the artificial heater is disabled and ohmic heating sustains the discharge.
2. Conductivity pre-conditioning: the electrical conductivity is temporarily scaled by a factor $\beta(t) > 1$ during the first N_{ramps} iterations. As the plasma begins to self-heat, $\beta(t)$ is smoothly reduced to unity. This approach avoids abrupt thermal ramps.
3. Analytic seed field: a prescribed, axisymmetric temperature profile is imposed initially (Fig. 3). With T frozen, the momentum equations are advanced to steady state, yielding a consistent velocity field. The temperature is then released, and the coupled system relaxes to the operating state.

In all three cases, the time-step controller dynamically adjusts Δt to ensure that successive temperature increments remain bounded and do not destabilise the pressure correction. The strategy that proved most effective was introducing an analytic seed field (3), and this was used for further analysis.

During development, three recurring difficulties were encountered:

1. Requirement for elevated temperatures – high temperatures are necessary to reach the conductivity threshold for self-sustaining ohmic heating. Under ambient conditions, the torch stabilises in a “cold” steady state, distinct from the desired hot operational state.
2. Velocity-field sensitivity – sharp gradients in the initial velocity distribution frequently caused instabilities at start-up.
3. Wall-temperature gradients – steep radial gradients near the wall triggered divergence if the initial thermal field was poorly conditioned.

To mitigate issues 2 and 3, an unstructured grid was introduced, providing enhanced resolution near the wall. To address issue 1, a high-temperature artificial field was

prescribed to seed the discharge (Fig. 3). The most effective approach combined boundary-temperature control with iterative refinement: the wall temperature was initially set above the operating value and then reduced stepwise toward 350 K. At each step, the velocity field was allowed to develop before carrying forward both temperature and velocity fields as initial conditions for the next iteration.

This staged procedure ultimately produced a stable high-temperature steady state, which was stored and reused as the initial condition for subsequent simulations under varied process parameters.

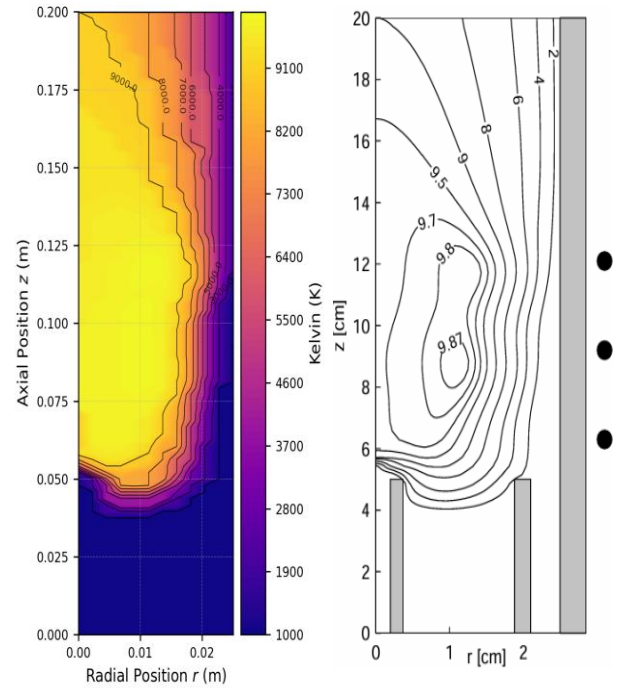


Fig. 3. Temperature profile initial condition (Left) and the temperature field ($T \cdot 1000$ K) obtained by Bernardi et al. [8] (Right).

3.4. Single particle insertion

The particle insertion framework was implemented using object-oriented programming in Python. A dedicated *Particle* class was constructed, allowing convenient grouping of parameters such as initial

diameter, velocity components, position, and temperature. The class included methods for evaluating the instantaneous relative velocity (U_R), Reynolds number (Re_p), drag coefficient (C_D), and convective heat transfer coefficient (h_c). Material properties for titanium were used, although the solver is generalisable to other materials.

The plasma velocity and temperature fields were provided as steady-state solutions from the torch CFD model. Particle equations were then integrated explicitly in time, with interpolation applied to obtain field values at arbitrary particle positions.

The system of differential equations governing the general particle property ϕ can be expressed by:

$$\frac{d\phi}{dt} = f_\phi(d_p, \rho_p, T_p, v_p, u_p, v, u, T) \quad (39)$$

where ϕ represents T_p , v_p , u_p , d_p or liquid fraction x . The function f_ϕ depends on the property ϕ and was derived from the equations provided in section 2.4. Using first-order explicit Euler time stepping:

$$\phi^{n+1} = \phi^n + \Delta t * f_\phi(X^n) \quad (40)$$

Since all the parameters are known at time step n a marching algorithm can be used to solve for the time history of parameter ϕ . Note, that the plasma temperature and velocity fields used are at steady state and therefore $T^{n+1} = T^n$. For potential transient torch simulations, however, the method can accommodate evolving background fields by advancing both solvers with the same time step Δt .

In some trajectories, particles encounter the inner wall of the torch. To simulate such interactions, a collision detection routine was implemented. When a tentative position exceeded the torch radius (R_{torch}) or crossed the axis, the particle position was corrected and velocities updated to represent bounce and friction effects.

At the torch wall:

$$u_{r,new} = -\epsilon u_r \quad u_{z,new} = f u_z \quad (41)$$

where ϵ and f are elasticity and friction coefficients, respectively (both close to unity for metallic particles).

And at the torch axis:

$$u_{r,new} = -u_r \quad (42)$$

Given the steep temperature gradients near the wall, it was assumed that particles impacting the wall were solidified due to rapid cooling. This justified treating wall collisions as elastic-inelastic bounces rather than continued melting.

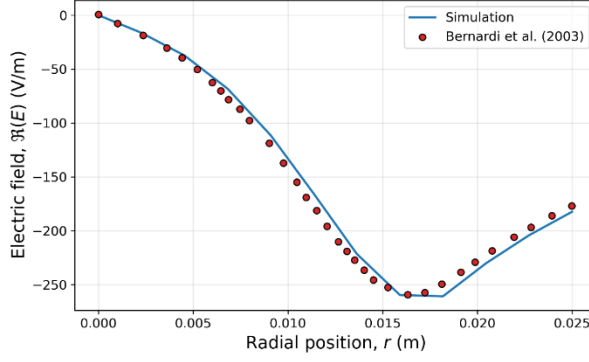
Algorithm 3 was used to solve single particle dynamics.

Algorithm 3: Particle Solver

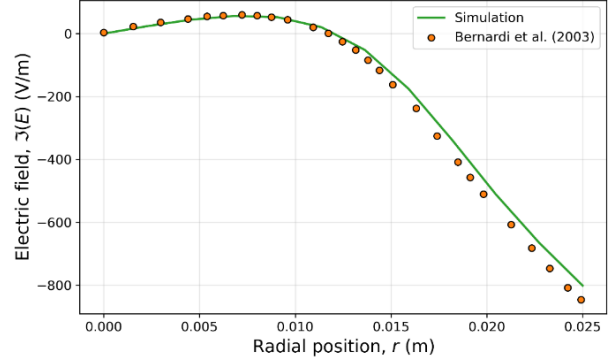
Inputs	Plasma temperature and velocity field. Initial particle temperature, diameter, and position. Time step, Δt
Start	
While:	Update position.
$t < t_{total}$	Update velocities. Calculate tentative velocities. From that, find tentative positions. <i>If</i> position outside domain correct the velocities to account for the wall. Energy Balance Check temperature. <i>If</i> particle temperature not at melting or boiling point update with sensible heat. <i>If</i> particle temperature at the melting point find the liquid fraction change and find the new diameter and particle area. <i>If</i> particle temperature at the boiling point find the new particle diameter and find the new particle mass.
End	

4. Results and discussion

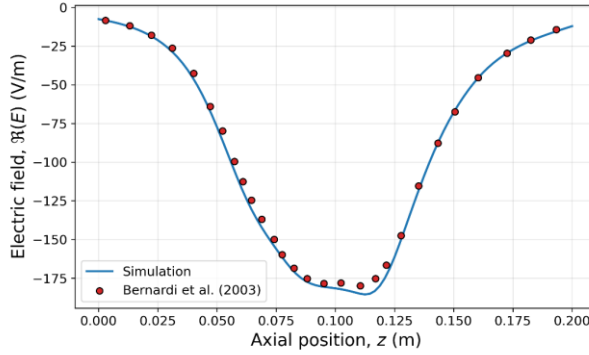
In this section, we present results from the Python model and compare them with literature. First, the electromagnetic fields are compared with those from Bernardi et al. [8]. The electromagnetic field is a function of the electric conductivity of the plasma gas, which in turn is a function of the temperature of the plasma gas. To ensure accurate comparison, an artificial temperature field was constructed to be the same as that used by Bernardi et al. [8] which is shown in Fig. 3. The same Tekna PL-50 ICP torch parameters were adopted and are provided in Table 1. Next, the thermo-fluid module on a staggered arrangement is verified against analytical laminar benchmarks for momentum and energy transport. The validated solver is then applied to a numerical domain that includes the carrier and sheath injection hardware of the PL-50 geometry to demonstrate physically plausible confinement and recirculation under operating boundary conditions and the cold steady-state. Subsequently, torch operation is examined across operating points: a steady-state baseline case is documented at 5 kW and systemic variations in coil power is introduced; additional studies show the importance of imposed swirl in the sheath flow on stability. Finally, a particle-insertion module is used to generate single-particle trajectories and melting / vaporization histories for titanium spheres over a range of diameters and injection radii. The results are summarised as compact spheroidization operating maps.



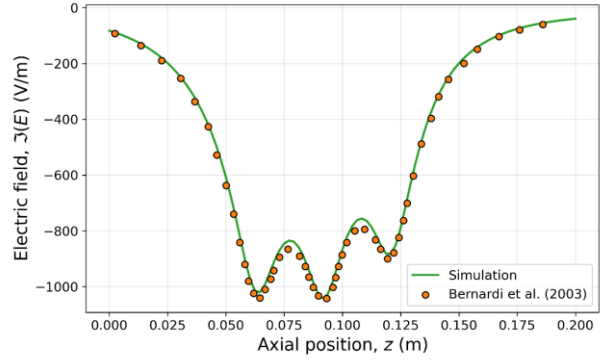
(a) Real part of the tangential electric field at $z = 102$ mm.



(b) Imaginary part of the tangential electric field at $z = 102$ mm.



(c) Real part of the tangential electric field at $r = 25$ mm.



(d) Imaginary part of the tangential electric field at $r = 25$ mm.

Fig. 4: Comparison of the tangential electric field with those found by Bernardi et al. [8].

4.1. Electromagnetic field

The complex electric and magnetic fields are compared on two standard lines, $z = 102$ mm and $r = 25$ mm, using a 12×97 structured evaluation grid with the temperature field from Bernardi et al. [8]. The procedure isolates the conductivity-driven electromagnetic response and enables like-for-like benchmarking of the present solver against literature case. The tangential electric field results are compared in Fig. 4 and the tangential magnetic field results are compared in Fig. 5.

The relative error of the Python model compared with the results found by Bernardi et al. [8] is provided in Table 4. The relative error remains less than 5%, which shows that the Python solver is consistent with literature. The error is probably derived from small discrepancies in the temperature field used in the Python model compared to that used by Bernardi et al. [8].

Table 4

Electric and magnetic field relative error.

Component	Mean relative error (%)
$Re[E_\theta]$ at $z = 102$ mm	2.85
$Im[E_\theta]$ at $z = 102$ mm	2.91
$Re[E_\theta]$ at $r = 25$ mm	1.68
$Im[E_\theta]$ at $r = 25$ mm	1.62
$Re[H_\theta]$ at $z = 102$ mm	3.13
$Im[H_\theta]$ at $z = 102$ mm	4.15
$Re[H_\theta]$ at $r = 25$ mm	1.28
$Im[H_\theta]$ at $r = 25$ mm	3.81

In literature the extended field approach is typically employed to solve the magnetic vector potential due to simpler boundary conditions that do not require an iterative approach [8, 10]. The EF approach uses an extended numerical domain that stretches far outside the ICP torch walls.

In this work the standard technique (ST), as outline in section 2.2., was employed to solve the electromagnetic field equations because it was found that with a good initial guess for the magnetic vector potential, the ST method is computationally more efficient than the EF approach due to the smaller numerical grid needed. A fine balance exists between the computational power needed for iterations compared to the computational power required to solve a larger set of linear equations. The computational time required between the ST and EF approaches are shown in Table 5. Note that the results are specific to this Python solver and computer hardware and that the results should be taken as indicative (refer to Table 10 for the workstation specifications).

Table 5

Comparison of the ST and EF solver times.

Method	Total time (s)
ST with $N_i=12$ and $N_j=97$	≈ 0.88
EF with $N_i=(12+15)$ and $N_j=(97+5)$	≈ 1.12
EF with $N_i=(12+20)$ and $N_j=(97+10)$	≈ 2.25

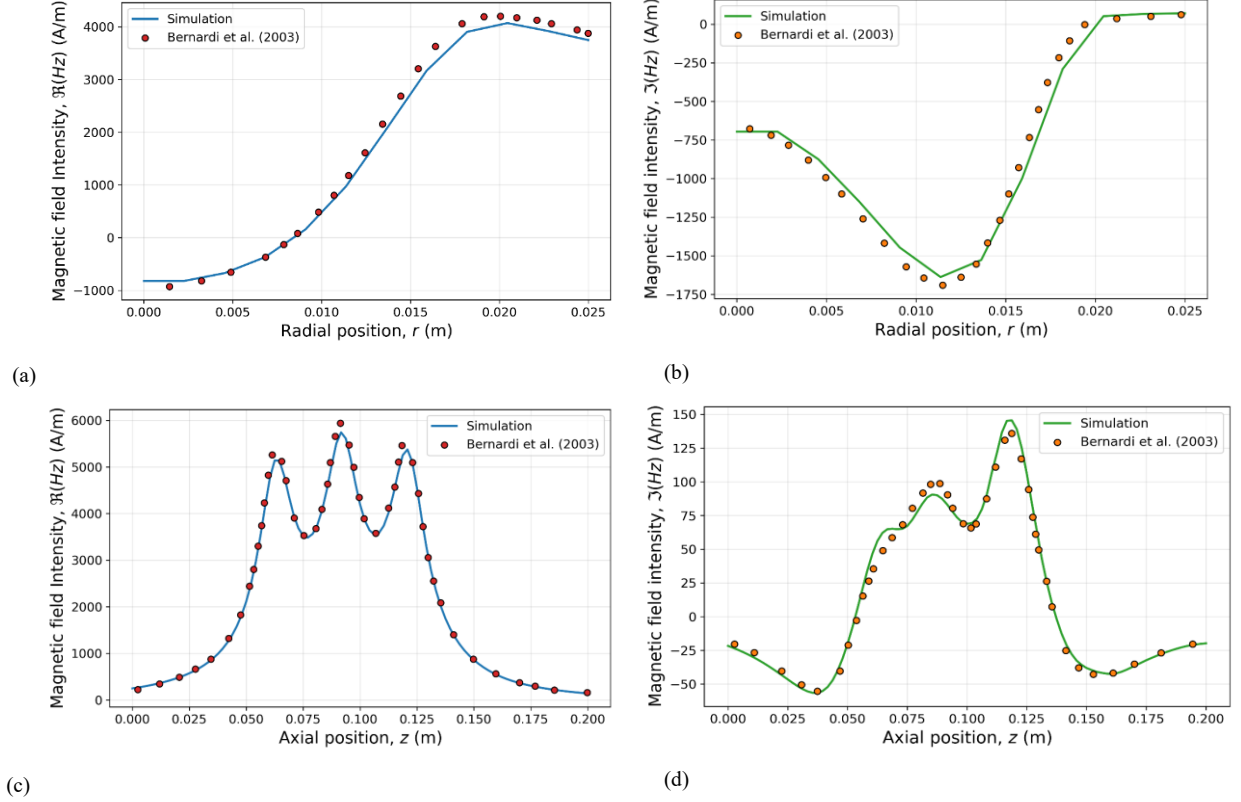


Fig. 5: Comparison of the tangential magnetic field intensity results.

The final steady-state electric and magnetic field contours, computed for the Tekna PL-50 geometry using the temperature distribution of Fig. 3 reveal the characteristic concentric lobes induced by the RF coils. The location of maxima and minima align with coil radii and axial positions, reproducing the contour patterns reported in literature [8, 10, 11].

4.2. Thermo-fluid

The thermo-fluid module solves the unsteady, compressible, axisymmetric Navier–Stokes and energy equations for argon in cylindrical coordinates. Two discretisation routes were explored. An initial finite-difference (FD) trial under isothermal conditions (1000 K) was used purely for diagnosis; despite reproducing basic velocity development, it exhibited pressure–velocity decoupling with a checkerboard pressure pattern, confirming the well-known instability of collocated FD schemes for this class of flows and motivating a change in approach.

The final solver adopts a conservative finite-volume (FV) formulation on staggered, hollow-cylindrical control volumes. This solver was verified against canonical laminar solutions in a cylinder of radius, $R = 25$ mm. For fully developed incompressible pipe flow, the axial velocity follows the Poiseuille parabola:

$$v(r) = v_{max} \left(1 - \left(\frac{r}{R}\right)^2\right) \quad (43)$$

and the thermal benchmark under constant wall temperature, T_w , for the dimensionless mean temperature follows:

$$\theta(z) = \frac{T_w - T_m(z)}{T_w - T_{m,inlet}} = \exp\left(\frac{-hPz}{\dot{m}c_p}\right) \quad (44)$$

where r is the radial position, z is the axial position, T_m is the mean temperature, h is the heat transfer coefficient, P is the perimeter of the torch, \dot{m} is the mass flowrate of argon gas, v is the axial velocity, and c_p is the heat capacity of the argon gas.

The inlet axial velocity was taken as 0.3 m/s and the temperature of the inlet gas was taken as 350 K. For the radial velocity profile, the temperature of the wall was set equal to 350 K. For the analytical thermal benchmark, the temperature of the wall was changed to 1050 K.

Against this reference, the computed axial mean-temperature profile matched with an average absolute error of 1.36 % while the radial velocity profile matched with an average absolute error of 0.507 %, confirming proper pressure-velocity coupling and conservation in the FV scheme. The comparison between the analytical and numerical results are presented in Fig. 6 and Fig. 7.

4.3. ICP torch results

The final velocity and temperature profiles within the ICP torch were initially unstable due to (1) excessive wall heating - suggesting that the cooling effect of the sheath gas was not fully resolved in the near-wall region, and (2)

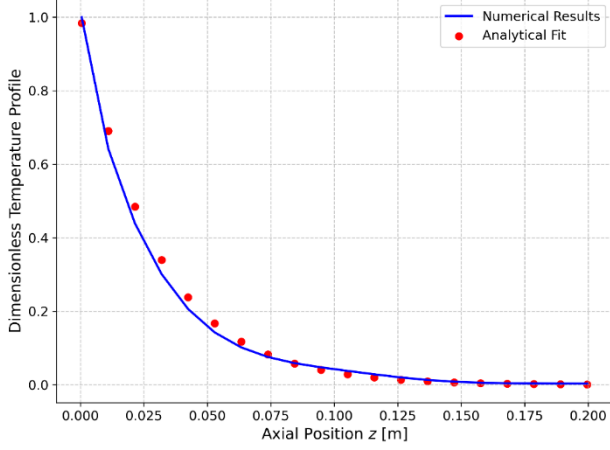


Fig. 6: Axial dimensionless temperature profile in the ICP torch.

a secondary wall eddy forming along the inner wall of the torch due to the action of the inwards pulling Lorentz force on the plasma. The electromagnetic field pushes ionized argon radially inward, which generates a localized low-pressure region just downstream of the coil. In turn, this low-pressure zone draws gas back from the outlet and from the sheath region, forming a secondary vortex. Both effects are not consistent with computational literature studies. The secondary eddy is depicted in Fig. 8, with the torch lying horizontally and its axis at the bottom. The sheath and injection probes are shown in black dotted lines. The secondary eddy around 125 mm is very clear – and it is because of the position of the coils around from 63 mm to 124 mm that causes the Lorentz force at this point to push argon gas inwards, creating that low pressure region which causes the secondary eddy as well as strong heating at the torch wall.

The way that the plasma-sheath interface was stabilized was via the introduction of an azimuthal velocity component at the sheath gas inlet – a scenario commonly referred to as swirl flow – which is typically used to

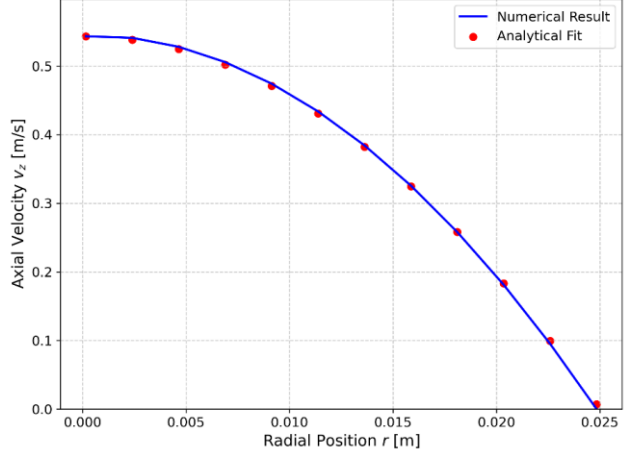


Fig. 7: Radial velocity profile of the axial velocity in the ICP torch at 0.16 m.

stabilize ICP torch operations. It is also known as dual injection [11]. This swirl generates a centrifugal force that acts radially outward, stabilising the plasma-sheath boundary and counteracting the Lorentz-force-driven entrainment of sheath gas into the torch core. Furthermore, this also ensures that the cool sheath gas remains at the wall of the torch, thereby preventing excessive heating from taking place. The additional centrifugal source term in the radial momentum equation (2) is simply:

$$+\rho \frac{u_{\theta}^2}{r} \quad (45)$$

where ρ is gas density, u_{θ} is the azimuthal velocity, and r is the radial coordinate.

A gentle swirl velocity of 5 m/s was applied at the sheath inlet, corresponding to a modest fraction of the maximum plasma velocity. The boundary conditions and the physical torch parameters are provided in Table 1 and Table 2, with the ICP torch run at 5 kW power. The velocity and temperature fields obtained at steady state for

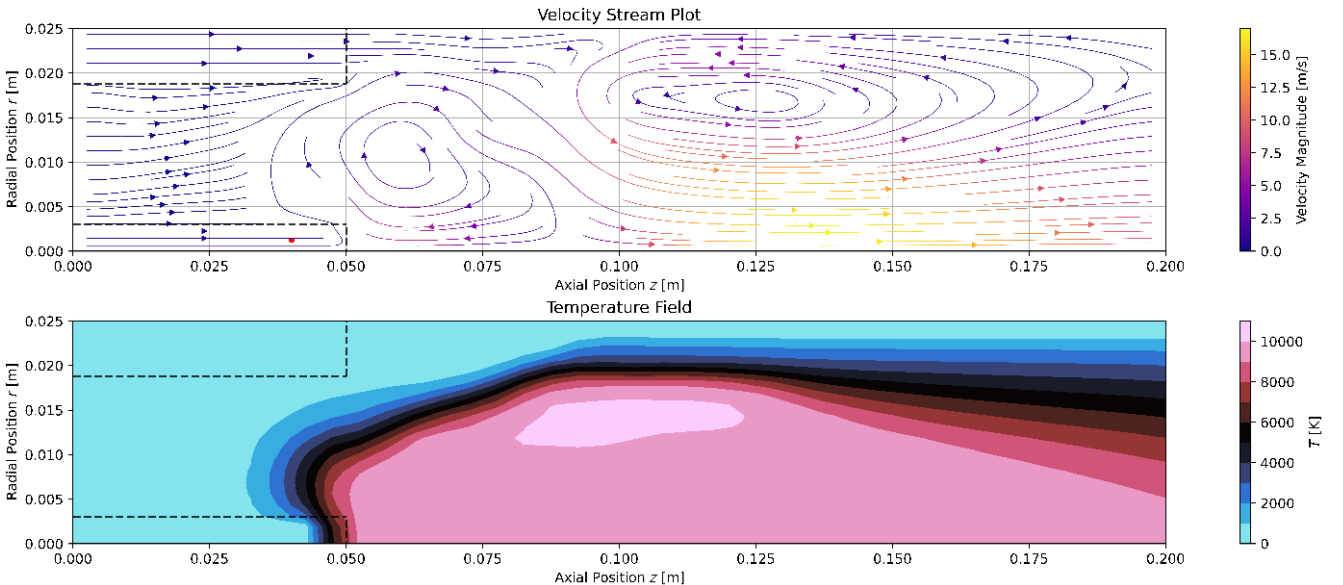


Fig. 8: Torch simulation at 5 kW showing the secondary eddy.

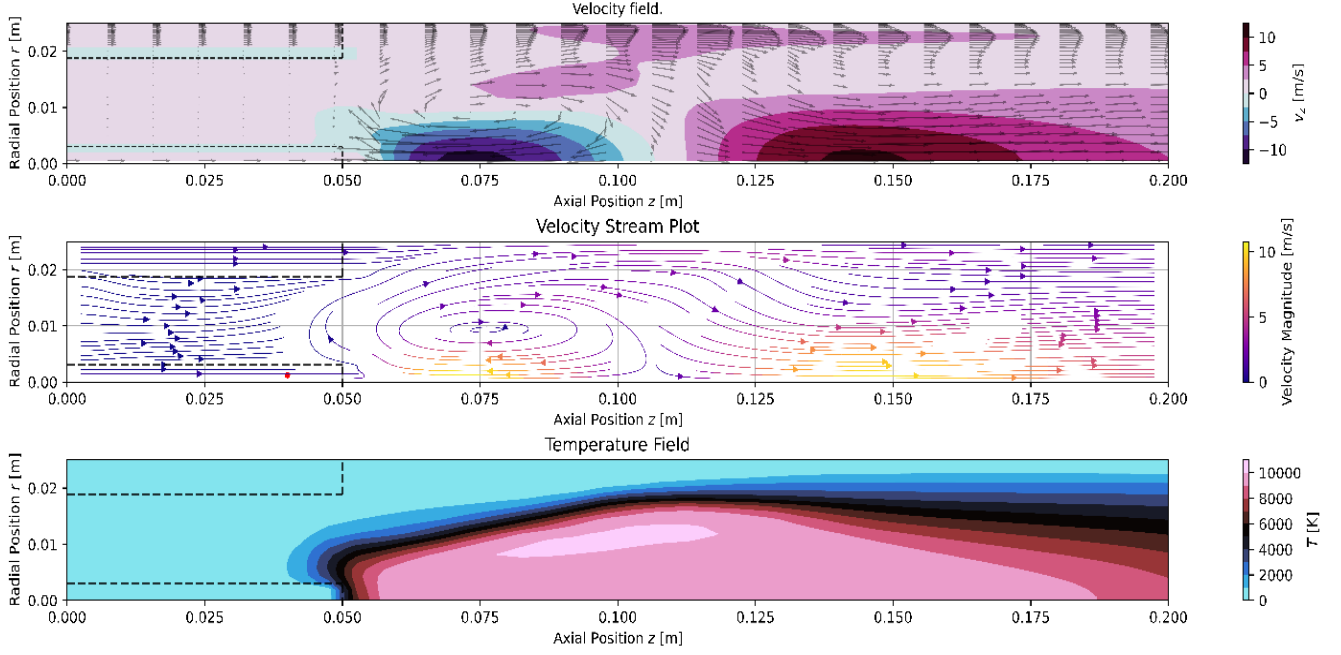


Fig. 9: 5 kW torch steady state after 3 seconds of simulation under dual injection conditions.

this stable simulation run are provided in Fig. 9. The maximum plasma temperature for the stable dual injection approach is 10,098 K, with streamlines and the primary recirculation eddy conforming to results obtained from literature [8, 10, 11].

As the torch power input increases, both the magnitude of the velocity and the absolute temperature inside the torch increases, however, not linearly, with higher power leading to smaller increases in the absolute temperature, as shown in Table 6.

Table 6

Maximum temperature and velocity in the ICP torch for different power inputs.

Power (kW)	Max. Temp. (K)	Max. Velocity (m/s)
5	10,098	11.42
10	10,563	19.10
15	10,888	20.31

Moreover, the maximum torch temperature and velocity is relatively independent of the main gas inlet velocity as shown in Table 7. The peak temperature differs by only 0.12 % and the velocity only by 5.73 % at 5 kW operating conditions.

Table 7

Maximum temperature and velocity in the ICP torch for different inlet flowrates.

Main flow rate (slpm)	Max. Temp.(K)	Max. Velocity (m/s)	Eddy position (relative shift)
1.5	10,088	10.79	Slightly upstream
3	10,098	11.42	Reference
6	10,092	11.05	Slightly downstream
12	10,077	11.43	Further downstream

4.4. Single particle spheroidization analysis

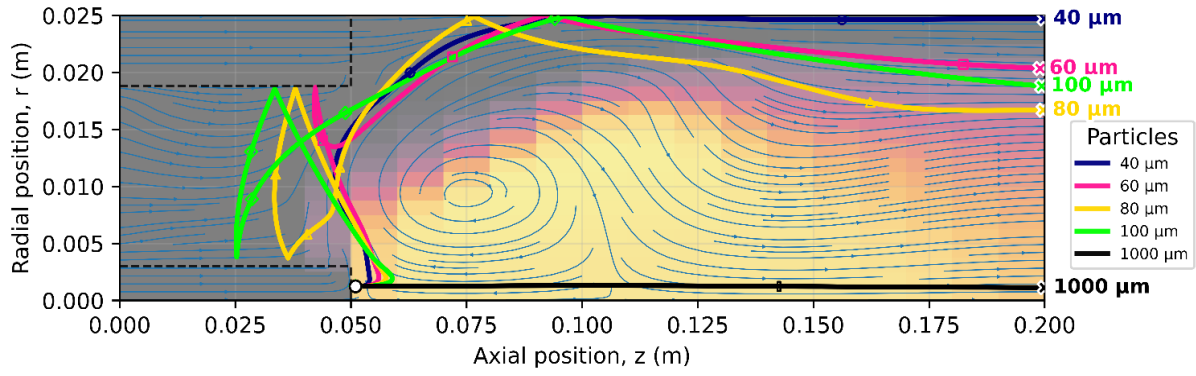
As noted, ICP torches are key for spheroidizing particles at Necsa.

To investigate this capability, titanium particles of different diameters were numerically injected into the simulated plasma flow field. The critical parameters controlling spheroidization are:

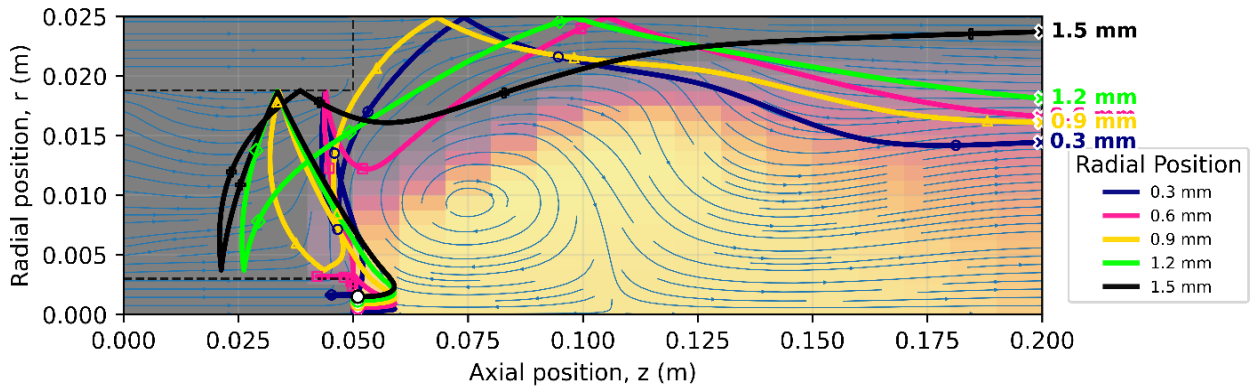
1. Initial particle diameter d_{pi} , which determines the volume-to-surface area ratio. This controls heat absorption relative to thermal mass.
2. Initial velocity v_{pi} , which influences the residence time and penetration depth into the plasma core.
3. Radial injection position r_i , which determines whether the particle is entrained in the central eddy or not.
4. Torch flow and temperature fields, which dictate the convective heat transfer, melting, and trajectories.

A particle is considered to have spheroidized when it reaches its melting temperature (T_{mp}) and fully melts, at which point surface tension drives it into a spherical droplet.

Trajectories were strongly diameter-dependent (Fig. 10 (a)). Particles smaller than 100 μm were entrained in the recirculating eddy, which reversed their axial motion before ejecting them downstream. This “bounce-back” effect increased residence time significantly, giving particles sufficient time to absorb heat and melt. In contrast, the 1000 μm particle travelled axially without significant deviation, resulting in a short residence time (≈ 0.075 s) insufficient for full melting.



(a) Impact of initial particle diameter on the particle trajectories for an initial radial position of 1.2 mm.



(b) Impact of initial particle radial position on particle trajectories for a 100 μm particle.

Fig. 10: Particle trajectory analysis for 5 kW operational power.

The detailed temperature and diameter history for the 80-micron particle is provided in Fig. 11 because it provides insights into the complex behaviour of medium-sized injected particles. The particle temperature initially increases drastically, and the particle rapidly melts and spheroidizes. Thereafter, the particle vaporizes, meaning that the final diameter of the particle is less than when it enters. The particle then solidifies, before it once again melts after bouncing against the torch wall and re-enters the plasma core and therefore it exits as a liquid droplet.

Vaporization becomes a large issue with particle spheroidization as it can cause large decreases in particle diameter and mass. Since the maximum temperature in the plasma is greater than 10,000 K and the vaporization point of titanium is only around 3,500 K, this will always

be a problem, especially for smaller particles. The changes in the diameters of the inserted particles of Fig. 10 (a) is summarised in Table 8 and shows that the smaller the particle, the larger the relative vaporization loss.

Table 8

Changes in diameter of titanium particle in the 5-kW torch.

Initial particle diameter (μm)	Final diameter (μm)	Residence time (s)	Spheroid?
40	31.38	0.134	Yes
60	52.88	0.155	Yes
80	75.55	0.263	Yes
100	97.52	0.249	Yes
1000	1000	0.075	No

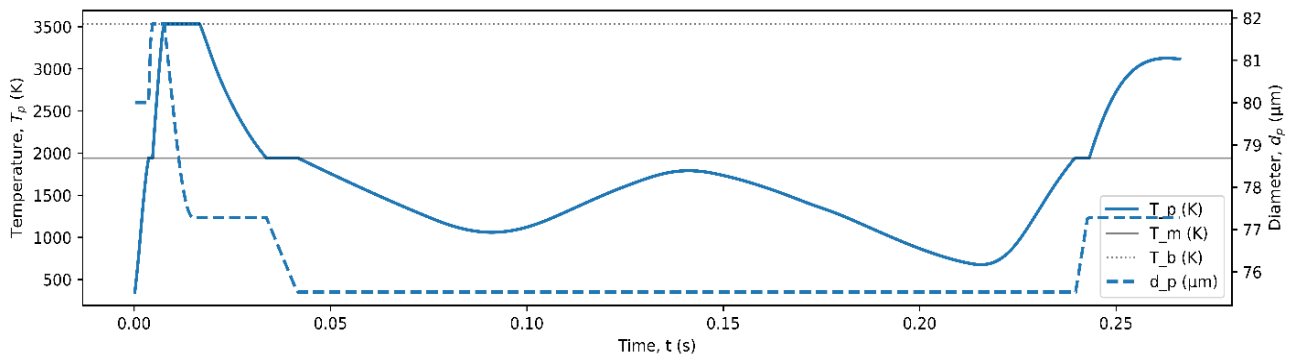


Fig. 11: The particle temperature and diameter profile for an 80-micron particle.

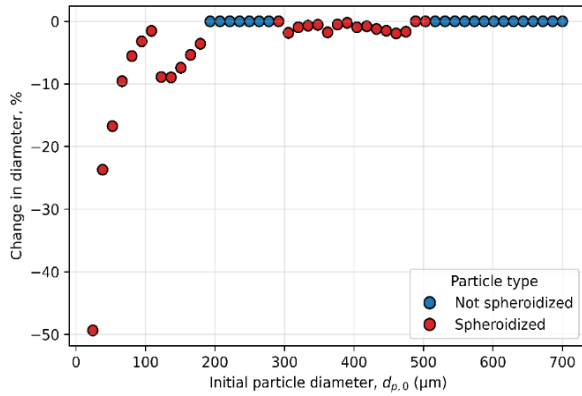
The dominant influence of particle size reflects the cubic scaling of volume with diameter. Small particles possess a much lower thermal mass relative to surface area, allowing rapid heating despite shorter residence times. In contrast, large particles require disproportionately more energy to reach melting temperature. These findings are consistent with the observations of Nam et al. [13], who also highlighted the strong role of particle size in spheroidization efficiency.

The radial injection position (r_i) was varied from 0.3 to 1.5 mm for 100 μm particles (Fig. 10 (b)) and while trajectories and exit positions differed noticeably, the final particle diameters varied by less than 1 % across the tested range (Table 9).

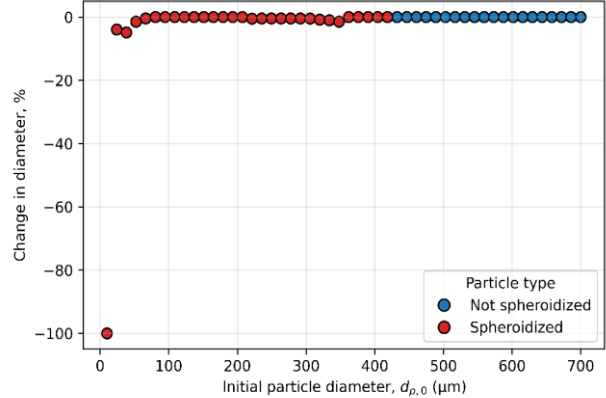
Table 9

Changes in diameter of a 100 μm titanium particle inserted at different radial positions.

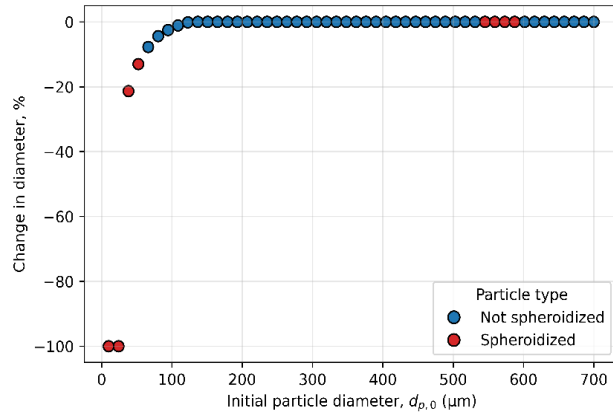
Initial radial position (mm)	Final diameter after cooldown (μm)	Residence time (s)	Spheroid?
0.3	96.96	0.309	Yes
0.6	97.66	0.400	Yes
0.9	97.40	0.307	Yes
1.2	97.41	0.250	Yes
1.5	97.62	0.256	Yes



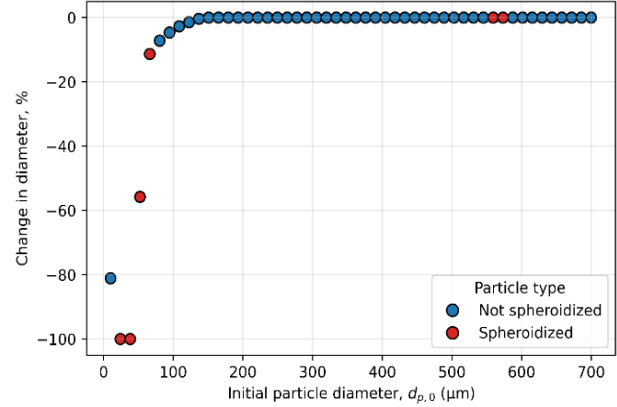
(a) Results for a torch operating at 5 kW.



(b) Results for a torch operating at 4.5 kW



(c) Results for a torch operating at 10 kW.



(d) Results for a torch operating at 15 kW.

Fig. 12: Spheroidization results and change in diameter for particles of different initial diameters for different power inputs.

The results confirm that radial position is a secondary parameter compared with particle diameter. While radial injection modifies the trajectory path length and exit location, it has negligible influence on the overall spheroidization outcome. This suggests that predictive accuracy depends more on capturing realistic temperature fields than on resolving fine details of the velocity field.

The spheroidization potential of particles was further analysed across a range of torch powers and inlet velocities. The results for four different torch operating power are provided in Fig. 12. At the base operating conditions (Fig. 12 (a)) particles up to approximately 500 μm were observed to spheroidize, while larger particles did not fully melt. Significant reductions in particle diameter are undesirable since they indicate vaporisation losses of titanium. Acceptable operating conditions were therefore identified in the 50-500 μm range, under the assumption that less than 50 % diameter reduction is acceptable. Particles in the intermediate range (200-300 μm) were expelled back through the inlet of the torch due to interaction with the backflow eddy. That is why these particles are indicated as not spheroidized since they are drawn back into the carrier inlet stream and excluded from spheroidization. Increasing the power to 10 kW and 15 kW almost completely removed the spheroidization operating window due to the stronger velocity fields (Fig. 12 (c) and (d)). The strong backflow eddy at this condition

caused particles in the 50-550 μm range to be drawn back into the carrier inlet stream, effectively excluding them from spheroidization. This shows that higher power operation does not expand the spheroidization range, but instead restricts it, due to adverse hydrodynamic effects (increased backflow and higher velocities). Fig. 13 (a) shows the particle trajectories at an operational power of 10 kW, where the 500 μm and 600 μm particles are expelled through the inlet of the torch due to the strong backflow at the carrier gas inlet. In contrast, Fig. 13 (b) shows the trajectories for an operational power of 4.5 kW, where none of the particles are ejected towards the inlet of the torch because the velocity field is much less aggressive. However, spheroidization can still occur reliably since the temperature field remains sufficient for melting (the peak temperature is 9,820 K).

Under these milder conditions, particles up to 400 μm spheroidize reliably, with no expulsion to the inlet (Fig. 12 (b)). Importantly, the reduction in diameter was also much smaller when spheroidization occurred, indicating lower vapourisation losses.

These results suggest that low-power operation is optimal for single-particle spheroidization, as the plasma remains hot enough to melt medium-sized particles while maintaining stable trajectories.

Lastly, it was found that changing the main carrier gas inlet velocity by factors from 0.5 to 4 has negligible changes in the operating window compared with baseline conditions. The strong recirculation eddy dominates

particle trajectories, rendering the effect of inlet velocity minor.

Note that all simulations were conducted under single-particle loading, serving as a proof-of-concept for spheroidization capability. Under industrial conditions with dense particle loading, particles will exchange momentum and absorb heat collectively, altering both velocity and temperature fields. In such cases, higher torch powers may be necessary to compensate for the increased heat demand.

4.5. Workstation specifications

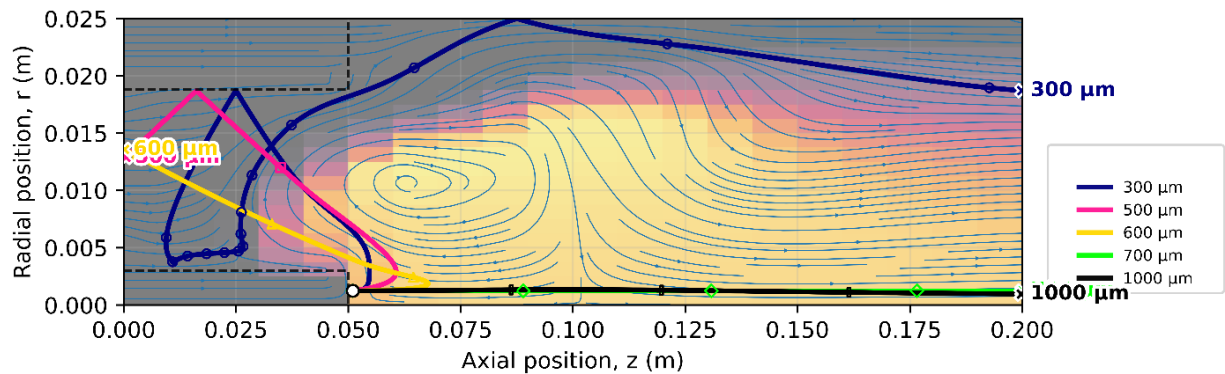
To conclude this study, the workstation specifications are provided in Table 10. The Python source code is available at the following link:

<https://github.com/Eisbergh/ICP-Torch-Modelling-University-of-Pretoria>

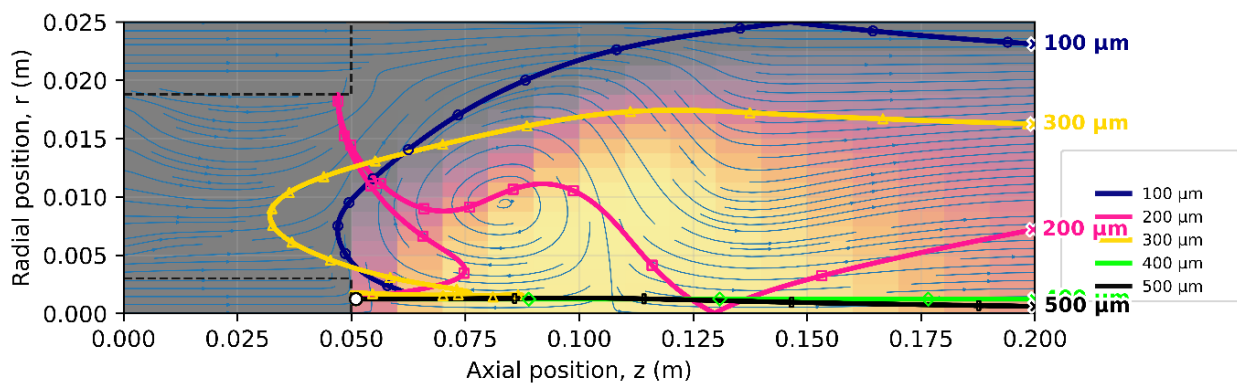
Table 10

Workstation specifications

Host system	Windows 11 Pro-64-bit, Intel i5 2.70 GHz processors, 32 GB RAM, NVIDIA GeForce RTX 3050, 5 GB, 6 cores, 12 logical processors
IDE	PyCharm Community Edition 2022.3.2
Python version	Python 3.8.3



(a) Particle trajectories for the torch at 10 kW.



(b) Particle trajectories for the torch at 4.5 kW

Fig. 13: Particle trajectory analysis for different operational power conditions.

5. Conclusion

This study developed a Python-based multi-physics solver for the Tekna PL-50 ICP torch, achieving accurate predictions of plasma temperature and velocity profiles with validation errors below 5% for electromagnetic fields and 1.4% for thermo-fluid benchmarks. Key findings demonstrate that swirl flow stabilizes the plasma-sheath interface, while higher power levels (10-15 kW) increase velocities but narrow the spheroidization window due to stronger recirculation eddies. The spheroidization of single titanium particles is dominated by diameter, with particles below 500 μm fully melting at 5 kW but experiencing up to 20% vaporization loss for sizes under 100 μm ; optimal conditions around 4.5 kW enable stable processing up to 400 μm with minimal loss. These results fulfil the objectives by providing an accessible alternative to commercial tools for simulating ICP dynamics and forecasting spheroidization behaviour, offering insights to enhance powder quality for additive manufacturing at Necsa. Future work should incorporate dense particle loading and experimental validation to refine industrial applicability.

CRediT authorship contribution statement

Hendrik J. Greeff: Writing – original draft, Writing – review and editing, Conceptualisation, Investigation, Software, Validation, Visualization, Formal Analysis, Methodology. **Samuel A. Iwarere:** Project administration, Writing – review and editing, Supervision. **Hertzog Bisset:** Project administration, Supervision.

AI Declaration

During the preparation of this work the author used ChatGPT in order to refine grammar and enhance professionalism of the text. After using this tool, the author reviewed and edited the content as needed and takes full responsibility for the content of the publication.

Acknowledgments

The authors gratefully acknowledge the support from the University of Pretoria's Department of Chemical Engineering. We also thank peers and family for their encouragement throughout this project.

References

- [1] Tong, J. B., Lu, X., Liu, C. C., Pi, Z. Q., Zhang, R. J., & Qu, X. H. (2016). Numerical simulation and prediction of radio frequency inductively coupled plasma spheroidization. *J. Appl. Therm. Eng.*, 100, 1198–1206.
- [2] Boulos, M. (2004). Plasma power can make better powders. *Met. Powder Rep.*, 59, 16–21.
- [3] Kuroda, S., Kawakita, J., Watanabe, M., Kim, K. H., Molak, R., & Katanoda, H. (2015). Current Status and Future Prospects of Warm Spray Technology. *J. Therm. Spray Technol.*, 20, 653–676.
- [4] Nam, J.-S., Park, E., & Seo, J.-H. (2019). Numerical Analysis of Radio-Frequency Inductively Coupled Plasma Spheroidization of Titanium Metal Powder Under Single Particle and Dense Loading Conditions. *Met. Mater. Int.*, 26, 491–500.
- [5] Moll, J. H. (2000). Utilization of Gas-Atomized Titanium and Titanium-Aluminide Powder. *JOM*, 52, 32–34.
- [6] Wang, J.-J., Hao, J.-J., Guo, Z.-M., & Wang, Y.-M. (2014). Preparation of spherical tungsten and titanium powders by RF induction plasma processing. *Rare Met.*, 34, 431–435.
- [7] Wei, W.-H., Wang, L.-Z., Chen, T., Duan, X.-M., & Li, W. (2017). Study on the flow properties of Ti-6Al-4V powders prepared by radio-frequency plasma spheroidization. *Adv. Powder Technol.*, 28, 2431–2437.
- [8] Bernardi, D., Colombo, V., Ghedini, E., & Mentrelli, A. (2003). Comparison of different techniques for the FLUENT-based treatment of the electromagnetic field in inductively coupled plasma torches. *Eur. Phys. J. D*, 27, 55–72.
- [9] Colonna, G. & D'Angola, A. (2016). *Plasma Modelling: Methods and Applications*. IOP Publishing Ltd.
- [10] Busse, C., Tsivilskiy, I., Hildebrand, J., & Bergmann, J. P. (2021). Numerical modelling of an inductively coupled plasma torch using OpenFOAM. *Comput. Fluids*, 216, 104807.
- [11] Xue, S., Proulx, P., & Boulos, M. I. (2001). Extended-field electromagnetic model for inductively coupled plasma. *J. Phys. D: Appl. Phys.*, 34, 1897–1906.
- [12] Punjabi, S.B., Das, T.K., Joshi, N.K., Mangalvedekar, H.A. and Das, A.K. (2010). The effect of swirl velocity on ICP torch simulation. *Journal of Physics: Conference Series*, 208(1), 012055.
- [13] Nam, J.-S., Park, E. & Seo, J.-H. (2020). Numerical analysis of radio-frequency inductively coupled plasma spheroidization of titanium metal powder under single particle and dense loading conditions. *Met. Mater. Int.*, 26, 491–500.